INVITED ARTICLE

High-Resolution Imaging With Large-Angle Elastically Scattered Electrons

S J Pennycook
Solid State Division
Oak Ridge National Laboratory
Oak Ridge, TN 37831-6024

Abstract

A new method for forming high-resolution images is described using large-angle elastically scattered electrons in a scanning transmission electron microscope. The imaging is incoherent so that there is no contrast from within an amorphous phase, no Fresnel fringe effects at interfaces, no lateral spreading of the lattice image, and minimal dependence on microscope focus and specimen thickness. The image is not a reconstruction of the object from the diffracted beams emerging from the sample, but, at least for thin crystals, is best thought of simply as a map, showing atomic resolution, of the scattering power of the sample. The scattering power for high-angle scattering is strongly dependent on atomic number Z giving the images a strong chemical sensitivity. Examples of semiconductor and superconductor materials are presented.

Introduction

Conventional high-resolution electron microscopy and conventional analytical electron microscopy are clearly distinct techniques, although in recent years it could be said that they have been moving toward a common goal. High-resolution imaging has been concerned with increasing its chemical sensitivity, while analytical microscopy has been concerned with improving its resolution, ideally to the atomic scale. Improved chemical sensitivity in a high-resolution image can be obtained by increasing the resolution beyond what is needed for simply resolving the lattice[1-3] and looking at the fine details of the phase contrast image. For higher sensitivity to impurity atoms diffuse imaging can be employed in which the lattice contrast is avoided.[4,5] It is probably fair to say that the extraction of chemical information from conventional phase contrast images is the most challenging aspect of high-resolution studies (see the excellent review by Bourret[6]). In conventional analytical electron microscopy the electron energy-loss technique has the best chance of achieving atomic resolution, since compared to x-ray detection, this technique minimizes the effect of beam broadening in the sample, has a high collection efficiency, and with the advent of parallel detectors also has a high detection efficiency. The achievable resolution will still be limited by the low cross section of many processes of interest and by the fact that their signatures often lie on a large background of many other events. Resolutions achieved to date have been at nanometer rather than atomic dimensions.[7,8]

High-angle elastically scattered electrons provide a means of bridging the gap between conventional imaging and analysis. Characterized by a cross section which is both reasonably high and strongly Z dependent, an image based on high-angle scattering can show both atomic resolution and chemical sensitivity. The Z-contrast method can be considered either as a high-resolution imaging technique with strong chemical sensitivity or as an analytical technique capable of atomic resolution. This will be demonstrated by the examples presented below.

Background

It has long been realized that if electrons scattered through high angles could be utilized in a microscope, then improved chemical sensitivity would result.[9] This is because the scattering factors become increasingly Z dependent at large angles approaching eventually the full Z^2 dependence of unscreened Rutherford scattering. In a STEM, these electrons can be utilized by placing an annular detector around the transmitted beam. Crewe and co-workers included these high-angle scattered electrons using an annular detector extending from low to high angles.[10,11] This intercepted a large fraction of the total elastic scattering giving an efficient image showing good Z contrast with which they were able to image single heavy atoms supported on light substrates. The contrast was sufficient to allow individual atoms of platinum and palladium to be distinguished.[12] In this case it is not beneficial to detect only high-angle scattered electrons, since this reduces the detection efficiency resulting in a noisier image.[13] For crystalline materials, however, it is critical to detect only high-angle scattered electrons,[14] since detecting the diffracted beams scattered at low angles introduces diffraction contrast effects which at best obscure and at worst totally mask the Z contrast.[15,16] As the scattering angle increases, coherent Bragg diffraction becomes increasingly attenuated and replaced with the thermal diffuse background. Eventually, no diffracted beams can be distinguished, the scattering becomes incoherent with an angular dependence, which becomes that of simple Rutherford scattering[17] (see Figure 1). The characteristic angle for this changeover from coherent to incoherent scattering is of the order of $(u^2)^{1/2} / \lambda$, where u^2 is the mean square atomic vibration amplitude. For Si at room temperature, this is ~80 mrad. The intensity scattered in the incoherent tail at high angles will still be sensitive to crystal orientation through the electron channeling effect. A beam incident parallel to a crystal plane or axis will be concentrated onto the atomic planes or columns, resulting in a higher scattered intensity at high angles than if the same beam was incident on the crystal in a random direction. Such crystallographic, orientation, or channeling effects are well understood from dynamical diffraction theory,[18] and form the basis of the recent lattice location techniques using characteristic inner-shell excitations.[19,20]

The intensity of the incoherently scattered electrons will also have a dependence on thickness. However, if sample thick-

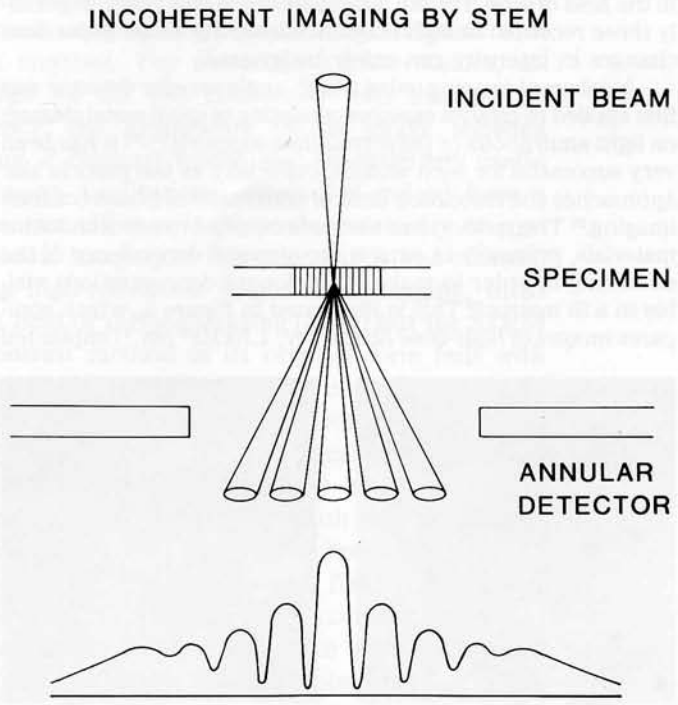

Figure 1. Schematic showing incoherent imaging in the STEM using a high-angle annular detector to collect the incoherent tail of the elastically scattered electron distribution.

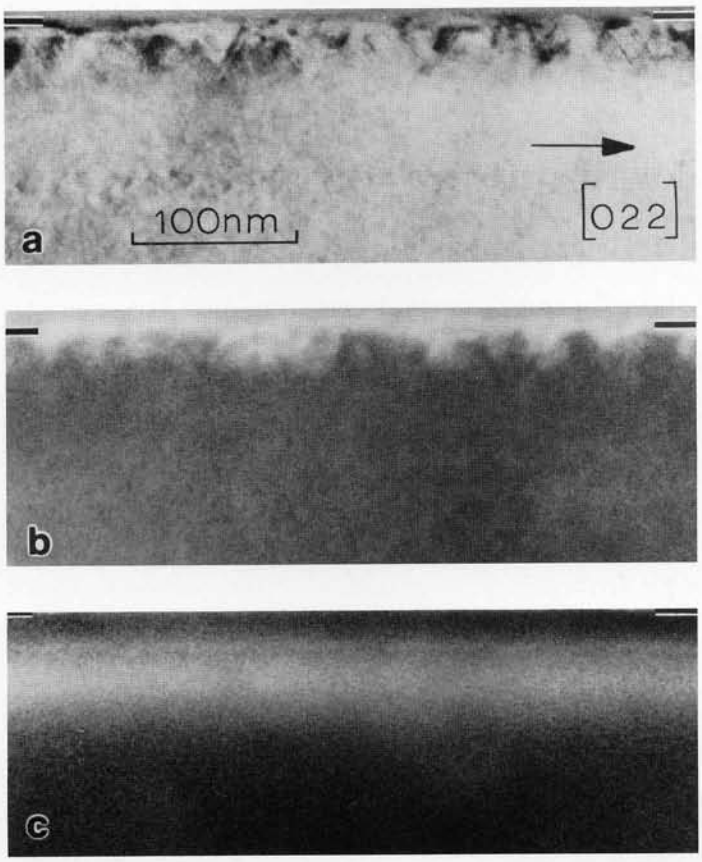

Figure 2. Cross-section images of Sb-implanted Si following solid phase epitaxy (SPE) growth; a) conventional bright-field image; b) STEM low-angle annular dark-field image showing diffraction contrast; c) STEM high-angle annular dark-field image showing Sb distribution via Z contrast.

ness variations are either gradual or non-existent, then this effect will result in changes of intensity of a large scale compared to the field of view. For the images shown in this paper, especially those recorded at high magnifications, thickness-dependent changes in intensity can safely be ignored.

Incoherent imaging using a high-angle annular detector was first applied to catalyst samples consisting of small metal clusters on light amorphous or polycrystalline supports.[16,21] It has been very successful for such studies, especially as the particle size approaches the resolution limit of conventional phase contrast imaging.[22] The method has also been applied to semiconductor materials, primarily to exploit the strong Z dependence of the scattering in order to make small dopant concentrations visible in a Si matrix.[23] This is illustrated in Figure 2, which compares images of high-dose Sb (80 keV, 1.5×10^{16} cm^{-2}) implanted Si following recrystallization in a furnace at 550°C for 40 min. The conventional TEM image (Figure 2a) clearly shows the interfacial breakdown which occurred 30 nm from the surface. It can also show the strains induced by the dopant and the twins, but gives no direct indication of the dopant distribution which caused the breakdown of epitaxial growth. Neither does the wide-angle annular detector image (Figure 2b), since Bragg beams reaching the detector dominate the contrast. However, by tilting away from the two-beam condition to avoid strongly exciting Bragg beams, and by increasing the inner detection angle to 65 mrad, the image in Figure 2c is obtained. This directly maps out the Sb concentration, even showing a fine band of high concentration dumped at the point where interfacial breakdown occurred. Such an image represents an elemental map, and can be directly quantified using appropriate screened cross sections.[24] The incoherent nature of the Z-contrast image is particularly useful for these studies of recrystallization and phase transformation, since the dopant is imaged independent of the phase of the Si matrix. Figure 3 illustrates this very well for the case of In (125 keV, 2×10^{15} cm^{-2}) implanted Si rapid thermally annealed at 700°C for 60 seconds. The conventional TEM image (Figure 3a) shows that epitaxial recrystallization occurred part way only, the remaining material being fine-grain polycrystalline Si. Precipitates of In are visible in the epitaxially grown Si, and the end-of-range damage below the original amorphous/crystalline interface can be seen. The Z-contrast image shows clearly that In precipitates are also present in the polycrystalline Si, and that interfacial segregation has occurred. A high concentration, both of precipitates and of In in solution, is seen just ahead of the crystallization front. Z-contrast studies showed clearly that the amorphous/polycrystalline transformation nucleates heterogeneously on In precipitates which form homogeneously in the highly doped amorphous Si.[25] The transformation proceeds in competition with epitaxial recrystallization,[26] and its associated interfacial segregation.[27]

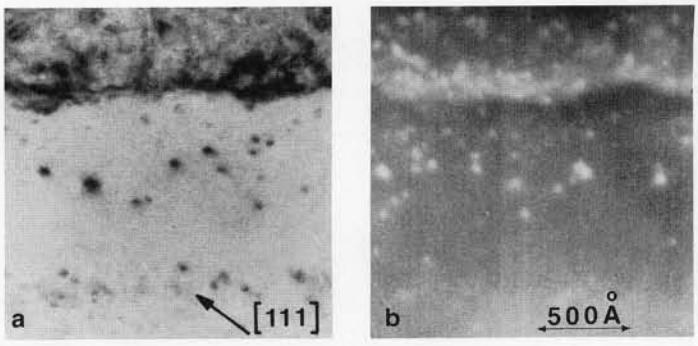

Figure 3. a) Conventional diffraction contrast TEM image, and b) Z-contrast STEM image showing In distribution after rapid thermal annealing of In-implanted Si.

Studies such as these showed clearly how high-angle elastic scattering could be usefully applied to many problems in materials science, exploiting its twin characteristics of strong Z-sensitivity coupled with the incoherent nature of the image.[28] This prompted speculation on the possibilities of high-resolution imaging based on high-angle elastic scattering, especially since the point resolution limit for incoherent imaging, 0.43 $C_s^{1/4}\lambda^{3/4}$, is significantly less than that for coherent imaging, 0.66 $C_s^{1/4}\lambda^{3/4}$.[29,30] Would it be possible to preserve the chemical sensitivity of high-angle scattering and simultaneously resolve the crystal structure? Clearly, in the limit of a very thin crystal this should be possible, although it was not so clear how the strong electron channeling effects set up by axial illumina-

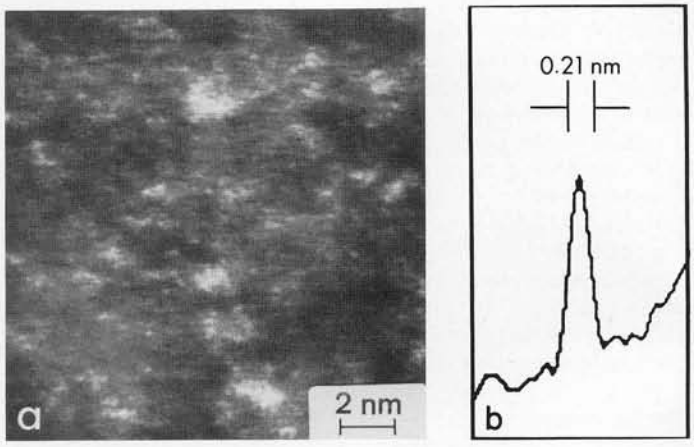

Figure 4. a) STEM image of uranium clusters on a thin carbon film; smallest spots are single atoms (100 keV, $C_s \sim 1.3$ mm, $\alpha \sim 11$ mrad, $\beta \sim 15$-150 mrad semiangles); b) intensity profile across single atom.

tion would manifest themselves. Such questions were answered using a VG Microscopes HB501 STEM operating at 100 keV and equipped with an ultrahigh resolution polepiece. For the theoretical C_s = 1.3 mm, an incoherent resolution limit of 0.22 nm was predicted. The performance was tested using a sample of single uranium atoms supported on a thin carbon film, and the results are shown in Figure 4. Single atoms are visible, and intensity profiles across them gave probe sizes (full-width, half-maximum intensity) in the range 0.21-0.24 nm, in excellent agreement with the theoretical expectation.[28] Attempts to resolve crystal lattices with high-angle scattered electrons have been very successful. Below are presented a number of examples of high-resolution images from semiconductor and superconductor materials, followed by a discussion on high-resolution Z-contrast imaging compared to conventional phase contrast imaging.

Semiconductor Materials

Viewed along the <110> direction, the elemental semiconductors appear as an array of zig-zag chains of atoms with a chain separation of 3.3Å for Si (center to center). This should be resolvable with a 2.2Å probe, although the two projected sites within each chain, separated by 1.4Å, would clearly not be resolvable. An electron beam incident in this direction will be strongly channeled along these chains, and the intensity scattered to high angles will depend on the channeling effect as well as the atomic number of the scatterer. The image will be given by the electron intensity at the atom sites weighted by a suitable cross section for high-angle scattering and integrated through the sample. For Si and Ge electron channeling, calculations[31] show that the flux is concentrated equally on the two projected sites within each chain, but is periodic with depth in the crystal, peaking at depths of $n\xi/2$, where ξ is the effective extinction distance under multibeam conditions. Since ξ is significantly less for Ge than for Si (approximately 6 nm compared to 10 nm), the channeling effect builds up faster in Ge than in Si. The faster flux buildup on the atomic columns will enhance the Z contrast seen at a Ge/Si interface in the thinnest regions of the sample. This is precisely the region where phase contrast imaging cannot distinguish the interface, as shown in Figure 5. A thin epitaxial film of Ge (possibly containing up to 10 at.% of Si) was grown on Si(100) by oxidizing a Ge-implanted wafer.[32] The Ge is rejected from the SiO_2, and has no time to diffuse into the Si. It segregates as a thin epitaxial film, which is clearly visible in the Z-contrast image in Figure 5b, but not seen in the phase

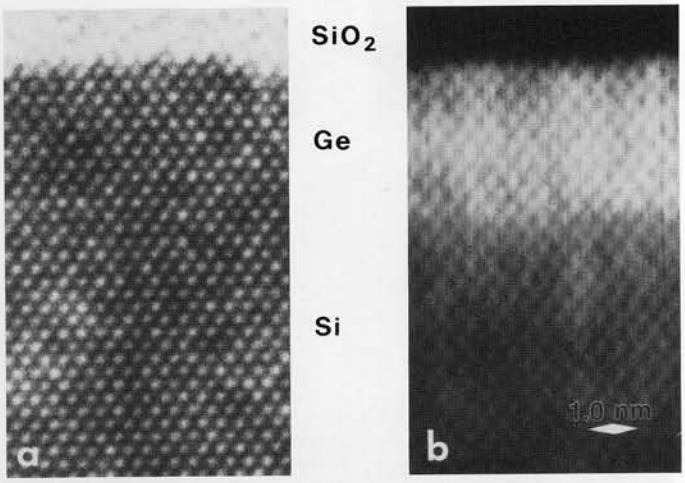

Figure 5. Thin region of an epitaxial film of Ge on Si grown by oxidation of Ge-implanted Si; a) phase contrast on conventional TEM; b) Z-contrast STEM image showing atomically sharp interface (α ~ 12 mrad, β ~ 50-150 mrad).

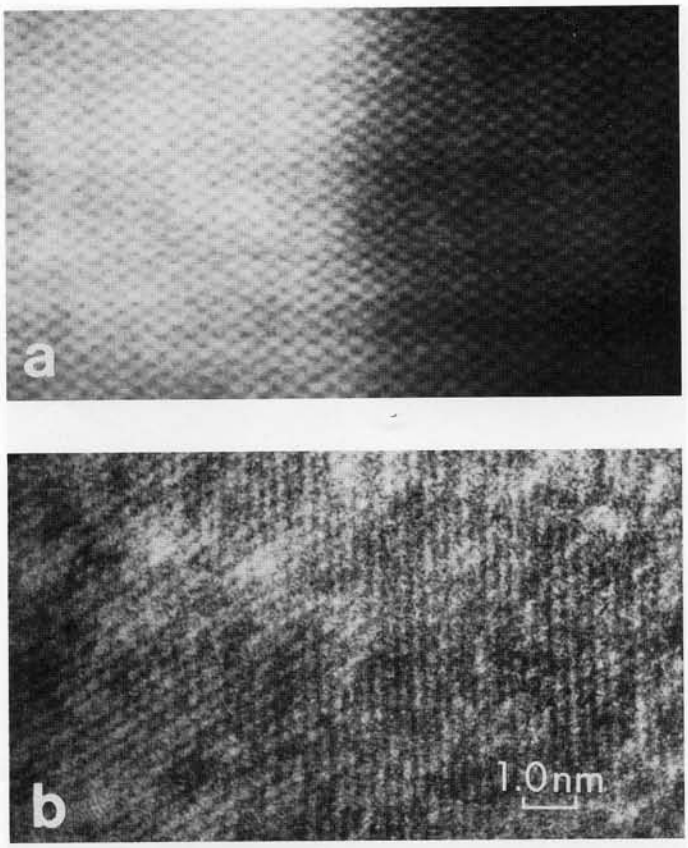

Figure 6. One interface in a MBE-grown $Si_{0.61}Ge_{0.39}/Si$ strained layer super lattice imaged by a) Z-contrast STEM showing chemically diffuse interface, b) phase contrast STEM.

contrast image from the same area. The phase contrast image is available simultaneously using the bright field detector of the STEM, although it is not a very efficient imaging mode in STEM and phase contrast lattice images are rather noisy. That shown in Figure 5 was taken on a JEOL 200CX to provide a comparable point-to-point resolution in the phase contrast image as in the Z-contrast image.

For thicker regions of specimen, the Ge layer is visible in a phase contrast image, although then the image necessarily averages over a greater distance parallel to the beam. Also, chemical interpretation at the atomic scale across the interface must be made by a full image simulation to include all the Fresnel effects at the interface. The Z-contrast image in Figure 5 directly shows atomic resolution chemical information. The bright spots show the location of the atom chains with the intensity depending on composition. There are no contrast reversals in the Z-contrast image, and it only appears over a narrow range of defocus. This is a consequence of the incoherent nature of the image; all the phase contrast effects of all beams are integrated up both in thickness and in angle so that, as noted before, the image depends on the thickness integrated electron intensity at the atom sites weighted by the cross section for high-angle scattering. Another consequence of the integration of phase contrast effects is that there is no contrast from within an amorphous phase. The SiO_2 layer above the Ge shows uniform dark contrast and the last Ge layers are clearly visible, whereas in the phase contrast image they are affected by the random contrast from the amorphous SiO_2. We plan to study lower dose implants to investigate the build up of the first monolayer of Ge. Also, with higher dose implants leading to thicker films, strain relaxation occurs through the introduction of misfit dislocations. Though they are often assumed to mark the interface, it would be interesting to see if, in fact, they ter-

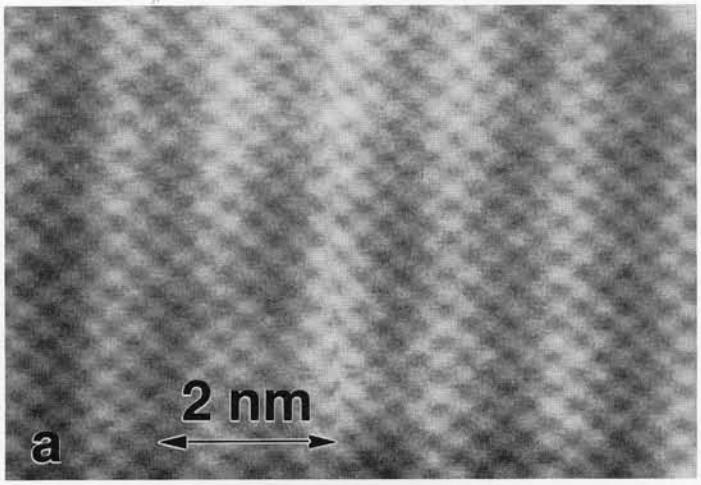

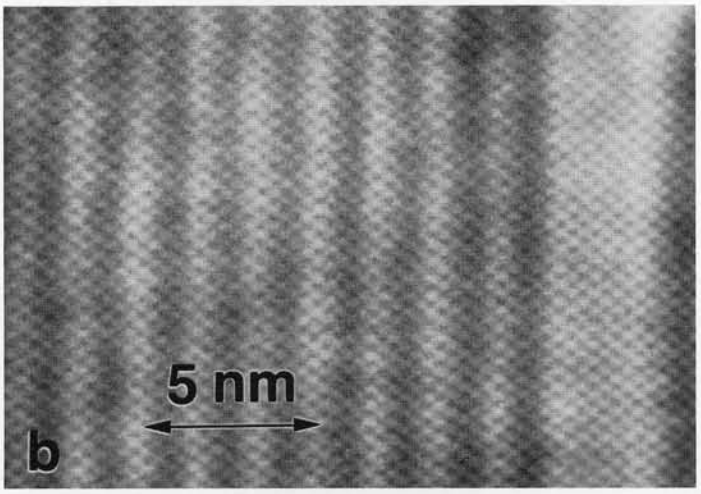

Figure 7. Part of an ultrathin multilayer $(Si_8Ge_2)_{100}$ showing a) interdiffusion on the monolayer scale, b) a stacking mistake in the superlattice, (α ~ 12 mrad, β ~ 75-150 mrad).

minated inside the Ge layer in order to minimize the local strain energy of the dislocation core.

An example of an interface which is chemically diffuse is shown in Figure 6. This is one interface in a Si_xGe_{1-x}/Si strained layer superlattice grown by MBE at a substrate temperature of 500°C and a deposition rate of 0.2-0.5 nm/s.[33] The Z-contrast image shows clearly that the interface is diffuse over a distance of 10Å and also that it is nonplanar. The phase contrast image (Figure 6b) was taken simultaneously on the STEM, and again the interface cannot be located. Slowing down the deposition rate to 0.02 nm/s gives more time for the flux arriving at the surface of the sample to migrate and form a smooth epitaxial film. Figure 7 shows images from part of an ultrathin superlattice grown this way.[34] The aim was to produce an artificial crystal $(Si_8Ge_2)_{100}$, that is, one hundred periods consisting of two monolayers of Ge followed by eight of Si. This should appear as one vertical row of bright dots due to the Ge double layer, separated by four darker rows of Si. The Z-contrast image in Figure 7a shows clear evidence of interdiffusion, the Ge double layer having broadened significantly. Figure 7b is a lower magnification image which shows the slight waviness of the layers, and also that the composition modulation is not quite parallel to the <100> direction. This is best seen by viewing along the layers at a low angle. Also visible at the right of Figure 7b is a stacking mistake which is clearly seen to be Ge rich. It was most likely caused by a failure of the Ge shutter to close when the Si shutter opened, since the two layers at each side of the mistake show contrast similar to the other Ge layers, but

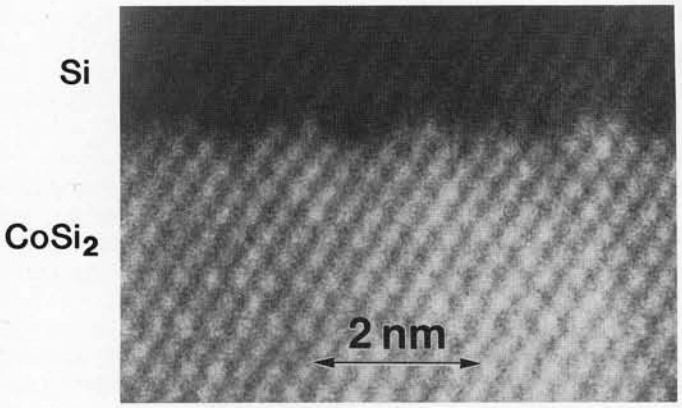

Figure 8. Z-contrast image of a $CoSi_2$/Si(100) interface showing interfacial reconstruction.

the area in between is wider and shows a contrast intermediate be-tween that of the Si and the Ge layers. It should be possible to quantify images such as this, and those seen in Figures 5 and 6, using image simulations combined with thickness measure-ments or with composition measurements in nonchanneling orientations, which can be obtained at reduced resolution by quantitative Z contrast or from x-ray analysis. It appears quite possible to obtain a column by column composition map across such interfaces.

Finally, Figure 8 shows a Z-contrast image of a $CoSi_2$/Si(100) interface produced by UHV evaporation of Co on clean Si(100) using a template method followed by homoepitaxial growth to a thickness of 6.5 nm.[35] Atomic resolution chemical information is clearly seen at the interface, and the image shows immediately the presence of an interface reconstruction, the periodicity in the <110> direction along the interface being four times that of the lattice. This reconstruction is clearly chemical in nature; the silicide structure appears to be correct right up to the last Co column, which is periodically located either in a complete {200} silicide plane or in the partially complete {200} layer above. The figure shows an intersection of two "domains" of the interface reconstruction; the three Co column-pairs in the partially complete {200} layer on the left of the

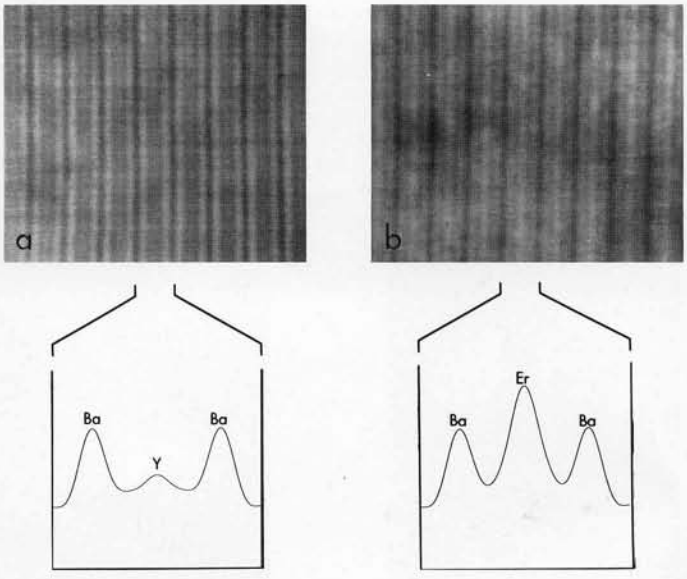

Figure 9. Planar Z-contrast image from a) $YBa_2Cu_3O_{7-x}$ and b) $ErBa_2Cu_3O_{7-x}$ single crystals (α ~ 6 mrad, β ~ 50-150 mrad). Line traces are calculated image intensity across the respective 1.19 nm unit cells in the c-direction assuming a Gaussian probe of 0.24 nm FWHM.

figure are out of sequence with the Co column-pair on the right, and are separated by a faint partially complete Co column-pair. Such domains are commonly observed. Although an interface reconstruction has been reported in a conventional phase contrast image of the same system,[36] it was typically not found during these observations. Here it was found everywhere. Either the conventional image is not sufficiently chemically sensitive or the reconstruction is quickly destroyed by irradiation at higher accelerating voltages. Channeling calculations indicate that the Z-contrast image from $CoSi_2$ is centered on the heavy Co atom sites in the <110> projection. Then the rigid shifts visible in the image are consistent with the interface structure proposed by Cherns, et al.,[37] for the isomorphous $NiSi_2$/Si(100) interface in which, at least for a flat interface, the Ni atoms retain eightfold coordination. They are not consistent with the model in which the Si atoms retain tetrahedral coordination, which, interestingly, was the model Cherns, et al., found to be consistent with their images of the $CoSi_2$/Si(100) interface. Note that in the incoherent Z-contrast image the rigid shifts observed are independent of defocus and sample thickness. At present, the driving force for the reconstruction is unclear.

Superconducting Materials

These materials tend to contain heavy atoms separated by relatively large distances, and are ideal for study by Z contrast. In fact, the first Z-contrast lattice images were obtained for the "1,2,3" superconductors $YBa_2Cu_3O_{7-x}$ and $ErBa_2Cu_3O_{7-x}$.[38] Observed under planar conditions parallel to the c-layer planes, Figure 9 shows quite clearly the strong chemical sensitivity. The Y plane (Z=39) is just visible in the Y123 material between the twin Ba (Z=56) planes, but when replaced with Er (Z=68) this plane becomes the brightest. In both materials the Cu(1) planes are darkest. Each plane is imaged with an intensity dependent on its projected scattering power. The calculated line traces in Figure 9 are obtained simply by convoluting an appropriate probe profile with the projected scattering power. It seems remarkable at first sight that such good agreement with the experimental image is obtained by ignoring all electron channeling effects at a thickness (~5 nm) well beyond the weak phase object limit for phase contrast imaging. This is because initially the channeling effect concentrates the electron flux equally onto the various planes, and only at significant thicknesses does it redistribute the flux and alter the relative intensity of the various planes.

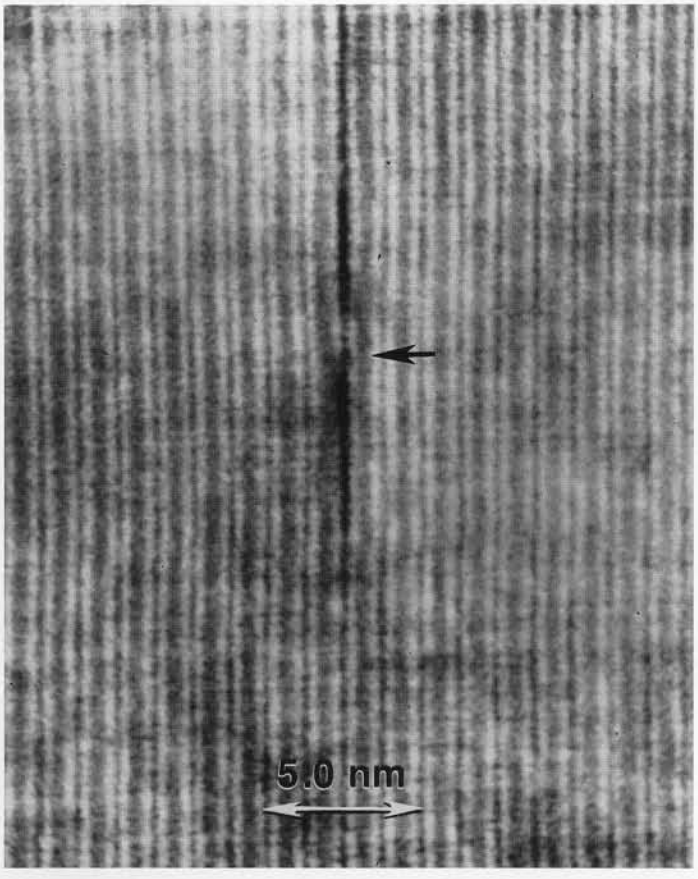

Figure 10. Planar defect in $YBa_2Cu_3O_{7-x}$ single crystal changing from substitutional type above the arrow to interstitial type below.

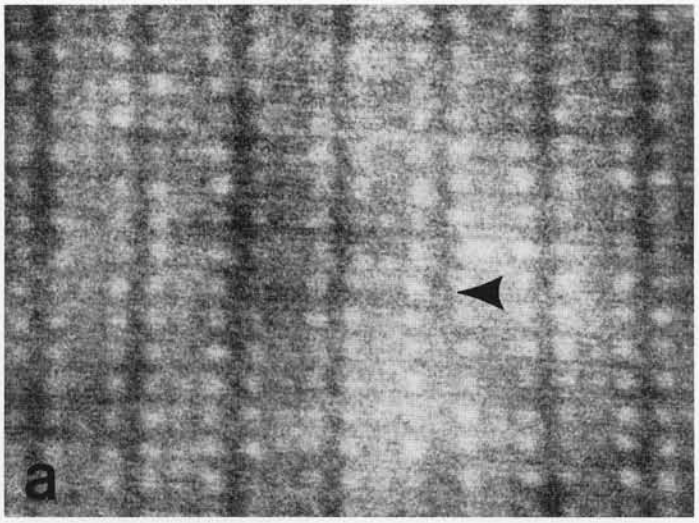

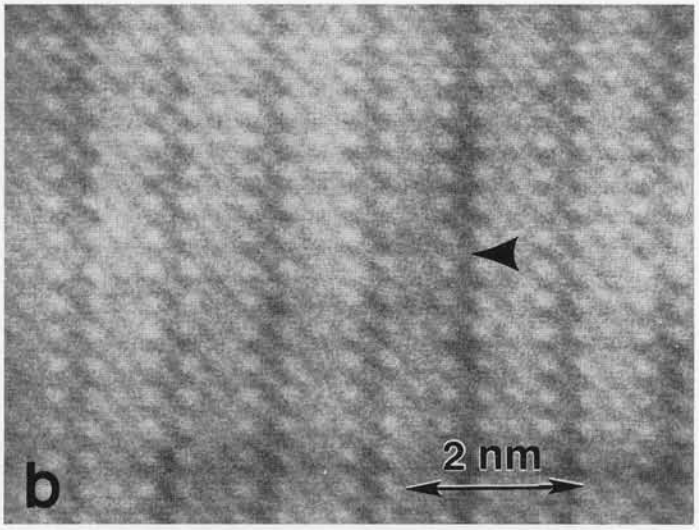

Figure 11. Axial image of a) substitutional and b) interstitial planar defects in $YBa_2Cu_3O_{7-x}$ (α ~ 12 mrad, β ~ 75-150 mrad).

Figure 10 shows an image of a planar defect in the $YBa_2Cu_3O_{7-x}$ crystal, which is located between the two Ba planes. Above the arrow it expands these planes a distance c/6, indicating an interstitial type defect, but below the arrow it does not, indicating a substitutional type of defect. The dark contrast indicates a light atom such as copper or carbon. In view of the existence of a $Y_2Ba_4Cu_8O_{20-x}$ phase,[39] it seems most likely that the interstitial defect comprises an extra CuO plane and can be considered an intrinsic defect, or a thin intergrowth of the 248 phase. This structure has also been proposed from phase contrast image simulations,[40,41] although in one case it was suggested to result from a degradation reaction.[41] In our experience, degradation results in the interstitial type defects, where clearly from the Z-contrast image some copper must be removed and

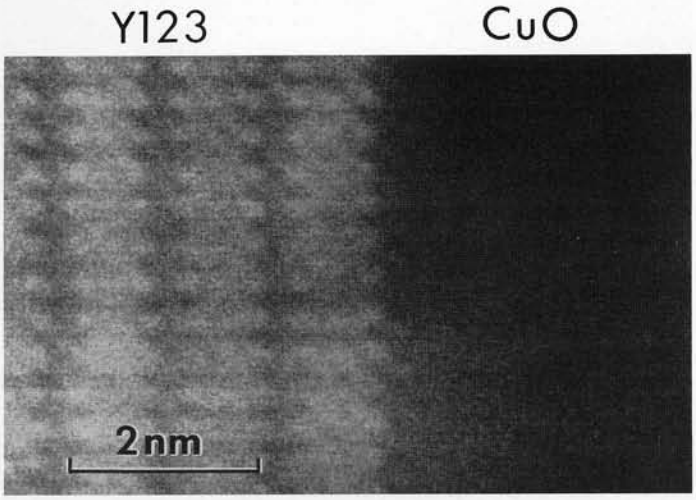

Figure 12. Grain boundary between $YBa_2Cu_3O_{7-x}$ and CuO in polycrystalline material, showing the superconductor terminating at the Cu(1) plane.

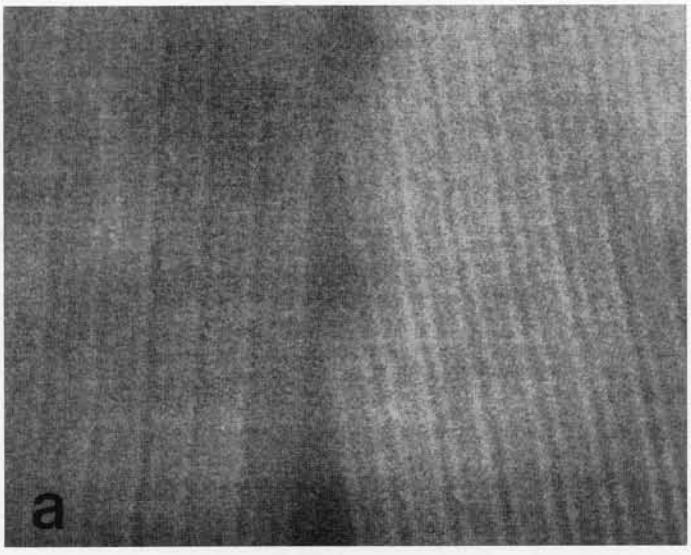

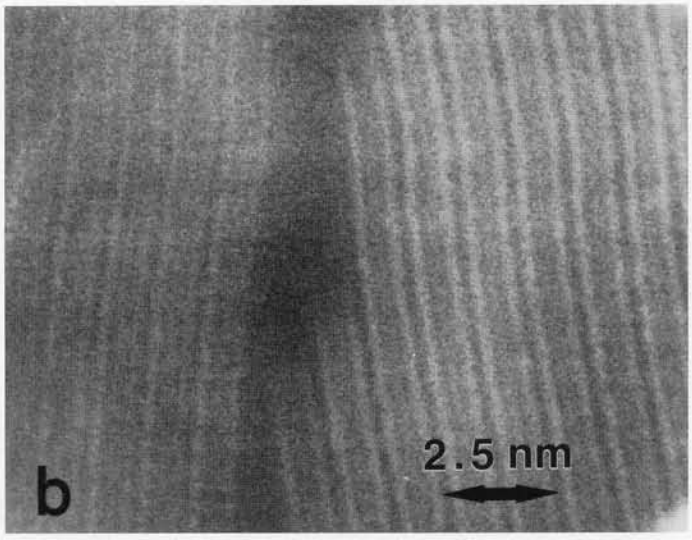

Figure 13. A low-angle tilt boundary in polycrystalline $YBa_2Cu_3O_{7-x}$. The boundary is parallel to the c-layer planes of one of the two grains, which are separated by triangular amorphous zones sometimes one (a), sometimes two (b) unit cells across. The Cu(1) plane is again the preferred termination plane. The slight waviness of the planes is due to specimen drift.

replaced with lighter atoms, most likely carbon. Figure 11 shows axial images of both kinds of defect. Again, the Cu(1) planes are the darkest in the image, but now the Ba columns are individually resolved and can be seen to move apart at the interstitial defect in (a), but are simply separated by a darker region for the substitutional defect in (b). The visibility of the Y columns and of the Cu(1) columns is better in the thinner region of the crystal at (b), although this is also slightly tilted.

The Cu(1) plane is clearly indicated as the weak link in the structure, and we have also observed that in polycrystalline material grains having a boundary parallel to the c-planes always terminate at this point. This is illustrated in Figure 12, which shows a grain boundary between a grain of $YBa_2Cu_3O_{7-x}$, which is imaged axially, and a grain of CuO, which is in an orientation in which its lattice is not resolved. Clearly, the superconductor chooses to terminate at the Cu(1) plane, and there are indications in the image that the Cu atoms at the interface are in their correct Cu(1) positions.

The same phenomenon is observed at the low-angle tilt boundary shown in Figure 13. Both grains again terminate after the Ba planes, although the Cu(1) sites are not visible due to imperfect axial alignment. The dark triangular regions are amorphous zones, sometimes one unit cell, sometimes two unit cells across to accommodate the tilt. Phase contrast microscopy studies of low-angle tilt boundaries have shown that the tilt is accommodated by an array of partial dislocations up to a critical angle of 5-7°, beyond which triangular amorphous zones are seen.[42] Since amorphous $YBa_2Cu_3O_{7-x}$ is not superconducting, such a result could well explain the measurements of critical currents across individual grain boundaries, which show these currents to be drastically reduced for tilts of only a few degrees.[43] It is of critical importance in determining the direction of future research in this area to know whether this effect is a structural relaxation, which is therefore avoided only by engineering low-angle boundaries, or whether it is due to a chemical segregation effect, which could be avoided by other means. This question can also be answered by Z-contrast imaging, simply by tilting the right hand grain in Figure 13 out of contrast. Then, crystalline and amorphous phases of the same composition will scatter at the same intensity, which is what was observed as shown in Figure 14. The scattered intensity is lower than for the grain which is still aligned, which shows enhanced scattering due to the channeling effect. To within a few percent, no contrast change is visible from the triangular regions, which are located to the right of the vertical part of the boundary, although compositional changes are visible further up the boundary. This rules out the possibility that the triangular regions are amorphous forms of the likely second phases such as BaO, CuO, Y_2O_3, Y_2BaCuO_5, or $BaCuO_2$. It also rules out significant changes in stoichiometry from the nominal $YBa_2Cu_3O_7$ composition. All indications are that this is an intrinsic structural relaxation of a chemically clean boundary, driven by the increasing grain boundary energy as the tilt angle increases and more dislocations per unit area are required.[44] This is exactly the kind of information needed for determining research directions in superconductor materials, and well illustrates the usefulness of the high-resolution chemical sensitivity of Z-contrast imaging.

Discussion

It is hoped that the examples presented here have demonstrated the two important characteristics of high-resolution Z-contrast imaging—the strong chemical sensitivity combined with the incoherent nature of the image. Both aspects are valuable for image interpretation. The incoherent nature means that the image is best not thought of as a reconstruction of the object from the various diffracted beams like a conventional phase contrast image, but as a high-resolution map of the channeling effect of the sample convoluted with the scattering power to high angles. It could be said that this represents a perfect reconstruc-

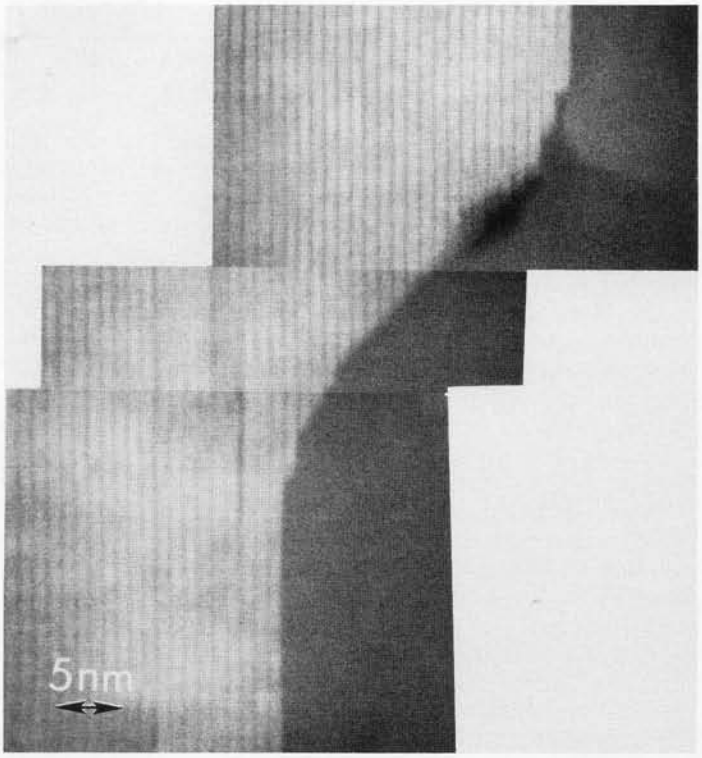

Figure 14. Z-contrast image showing no chemical changes between the triangular amorphous zones and the crystalline region of the right-hand grain of $YBa_2Cu_3O_{7-x}$ of figure 13.

tion, a "lensless" reconstruction inside the crystal of all the diffracted beams, although it seems simpler to think in terms of electron intensities in real space. This simple view of the imaging process ignores the coherent nature of the incident probe, and this aspect needs further consideration. However, electrons incident at the higher angles in the probe will tend to excite Bloch waves which are not peaked close to the atom sites. Since only the tightly bound Bloch waves will contribute significantly to the high-angle scattering, there seems reason to believe that the angular divergence could be ignored at least for a qualitative image simulation. Calculations on the superconductor material do show good agreement between experimental images at various sample thicknesses and images simulated by ignoring the angular dependence.[45] This approach may save significant computing time and make simulations of Z-contrast images as efficient as simulation of phase contrast images.

Compared to phase-contrast imaging, it must be true that the effective integration of phase-contrast effects in the Z-contrast image must result in less sensitivity in particular cases, most likely for light atoms. High resolution Z-contrast imaging should be viewed as complementary to phase-contrast imaging rather than as a replacement. Its advantages are in interpretability, that the likely atomic structure and chemistry are suggested more clearly from the image so that perhaps fewer possible models are suggested for image simulation. The incoherent nature of the image results in minimum dependence on sample thickness and microscope defocus, with no Fresnel fringe affects at interfaces, no lateral spreading of lattice fringes, and no "random" contrast from amorphous phases. It appears that atom positions are seen independent of thickness and defocus with an intensity which is chemically sensitive. It may even be possible to solve many structures without image simulation. These points will become clearer through further experiments and image calculations, and a better understanding of this new high-resolution imaging technique will be obtained.

Acknowledgments

It is a pleasure to thank my colleagues M F Chisholm, O W Holland, and D E Jesson for collaborations and discussions, M M J Treacy for loan of the resolution test sample, D C Houghton and J -M Baribeau for provision of the MBE-grown superlattices, S M Yalisove for provision of the silicide film, C W Boggs, J T Luck, and T C Estes for technical assistance, and VG Microscopes for design of the ultrahigh resolution polepiece and tilting holder, fully meeting all expectations. This research was sponsored by the Division of Materials Sciences, US Department of Energy, under contract DE-AC05-84OR21400 with Martin Marietta Energy Systems, Inc.

References

1. P M Fields and J M Cowley, Acta Cryst A 34, 103 (1978).
2. L A Bursill and Shen Guan Jun, Optik, 66 251 (1984).
3. A Ourmazd, J R Rentschler, and D W Taylor, Phys Rev Lett 57, 3073 (1986).
4. R W Glaisher and A E C Spargo, Inst Phys Conf Ser No 68 185 (1984).
5. J H Rose and R Gronsky, MRS Symp Proc 62 57 (1986).
6. A Bourret, MRS Symp Proc 138 and 139, (in press).
7. M Scheinfein and M Isaacson, J Vac Sci Technol B 4 326 (1986).
8. P E Batson, K L Kavanagh, C Y Wong, and J M Woodall, Ultramicroscopy 22, 89 (1987).
9. V E Cosslett, p 271 in Quantitative Electron Microscopy, ed by G F Bahr and E H Zeitler (Williams and Wilkins, Baltimore, 1965).
10. A V Crewe and J Wall, J Mol Biol 48 375 (1970).
11. A V Crewe, J P Langmore, and M S Isaacson, p 47 in Physical Aspects of Electron Microscopy and Microbeam Analysis, ed by B M Siegel and D R Beaman (Wiley and Sons, New York, 1975).
12. M S Isaacson, D Kopf, M Ohtsuki, and M Utlaut, Ultramicroscopy 4, 101 (1979).
13. C J Humphreys, A Hart-Davis, and J P Spencer, Eighth Int Congr on Electron Microscopy, Canberra 1, 248 (1974).
14. A Howie, J Microsc 117, 11 (1979).
15. A Donald and A J Craven, Phil Mag A 39, 1 (1980).
16. M M J Treacy, A Howie, and C J Wilson, Phil Mag A 38, 569 (1978).
17. C R Hall and P B Hirsch, Proc Roy Soc A 286, 158 (1965).
18. D Cherns, A Howie, and M H Jacobs, Z Naturforsch 28a, 565 (1973).
19. J C H Spence and J Tafto, J Microscopy 130, 147 (1983).
20. S J Pennycook, Ultramicroscopy 26, 239 (1988).
21. M M J Treacy, p 185 in Scanning Electron Microscopy/1981, ed by O Johari, (SEM, Inc, AMF O'Hare, Chicago, 1981).
22. M M J Treacy and S B Rice, J Microsc (in press).
23. S J Pennycook and J Narayan, Appl Phys Lett 45, 385 (1984).
24. S J Pennycook, S D Berger, and R J Culbertson, J Microsc 144, 229 (1986).
25. S J Pennycook, R J Culbertson, and S D Berger, MRS Symp Proc 100, 411 (1988).
26. E Nygren, J S Williams, A Pogany, R G Elliman, G L Olson, and J C McCallum, MRS Symp Proc 74, 307 (1987).
27. J S Williams and R G Elliman, Appl Phys Lett 40, 266 (1982).
28. S J Pennycook, Ultramicroscopy (in press).
29. O Scherzer, J Appl Phys 20, 20 (1949).
30. M G R Thomson, Optik 39, 15 (1973).
31. S J Pennycook, Scanning Microscopy 2, 21 (1988).
32. O W Holland, C W White, and D Fathy, Appl Phys Lett 51, 520 (1987).
33. D C Houghton, D J Lockwood, M W C Dharma-Wardana, E W Fenton, J -M Baribeau, and M W Denhoff, J Cryst Growth 81, 434 (1987).
34. J Lockwood, M W C Dharma-Wardana, G C Aers, and J -M Baribeau, Appl Phys Lett 52, 2040 (1988).
35. S M Yalisove, R T Tung, and J L Batstone, MRS Symp Proc 116, 439 (1988).
36. D Loretto, et al, MRS Symp Proc 139, (1989) [in press].
37. D Cherns, C J D Hetherington, and C J Humphreys, Phil Mag A 49 165 (1984).
38. S J Pennycook and L A Boatner, Nature 336, 565 (1988).
39. P Marsh, et al, Nature 334, 141 (1988).
40. D Domenges, M Hervieu, C Michel, and B Raveau, Europhys Letts 4, 211 (1987).
41. H W Zandbergen, R Gronsky, and G Thomas, Phys Stat Sol (a), 105, 207 (1988).
42. M F Chisholm and D A Smith, Phil Mag (in press).
43. D Dimos, et al, Phys Rev Lett 61, 219 (1988).
44. M F Chisholm and S J Pennycook, Phys Rev Lett (in preparation).
45. S J Pennycook, MRS Symp Proc 138 and 139 (in press).